Finite strain analysis of wood species under compressive failure due to kinking

L. Benabou *

Laboratoire d'Ingénierie des Systèmes de Versailles (LISV), Université de Versailles Saint-Quentin, 45 avenue des Etats-Unis, 78035 Versailles, France

ARTICLE INFO

ABSTRACT

Finite element analysis of kink band formation in wood is carried out using an anisotropic failure criterion. The criterion is capable of describing the mixed mode I/mode II crack development observed in the kinked region. The evolution of cracking is simulated with the help of the so-called smeared crack approach. As for the finite rotation of the fibers in the kinked material, it is implemented in the finite element code through a hypo-elastic law characterized by an objective derivate using the rotation of the fibers. This formulation enables to follow strictly the matter under finite strain; which means that the evolution of the orthotropic directions is correctly described.

Numerical results, such as the predicted load carrying capacity of wood under compression and its post-cracking behavior, prove to have a good agreement with the experimental observations. Further, the applicability of softening orthotropic plasticity under finite strain conditions for simulating compressive failure modes in wood is established.

© 2011 Elsevier Ltd. All rights reserved.

1. Introduction

Failure by kinking in wood has many similarities with kink banding in fiber reinforced composites. In the case of uniaxial composites, it was found that the compressive peak strength is governed both by local imperfections causing small misalignments of fibers and by plastic yielding in the matrix (Budiansky, 1983; Budiansky and Fleck, 1993; Moran et al., 1995; Kyriakides et al., 1995; Daniel et al., 1996). It has also been established that the transverse dilatancy of the material is a key factor that fixes the kink band orientation in fibrous materials (Budiansky et al., 1998; Christensen, 2000; Vogler et al., 2001) and in layered structures (Wadee et al., 2004). These are mainly the same parameters that account for the observed compressive strength and kink band inclination in wood species under compression (Poulsen et al., 1997; Da Silva and Kyriakides, 2007; Benabou, 2008, 2010). Additionally, it is worth mentioning the developments of Jensen and Christoffersen (1997) and Jensen (1999) who propose a kink band formation model for fiber composites based on the J₂-deformation theory and make additional in-depth studies on band broadening. Also, recent finite element simulations have been carried out to describe the failure of fiber composites by kinking (Sorensen et al., 2009; Veluri and Jensen, 2010).

Although wood species, under compression parallel to grain, exhibit deformation characterized by well-defined bands of bent fibers in the same way as fiber composites, their microstructure is much more complex. On the microlevel, wood can be regarded as an orthotropic body with three axes of orthotropy denoted *L*, *R* and *T* (Fig. 1a). The longitudinal direction *L* is parallel to the central axis of the tree and is the direction along which the most abundant type of cells found in wood are oriented. These cells, presenting tubelike structures and being the major structural elements of most species, are referred to as fibers for the sake of simplicity. The radial direction *R* and the tangential direction *T* are oriented respectively along the normal and the tangent to the growth rings of wood. Fiber misalignments observed in wood are essentially due to the so-called ray cells much smaller in size than the longitudinal fibers and located in the plane perpendicular to the trunk (along the radial direction *R* of wood) as schematized in Fig. 1b. In comparison with manufactured composites where defects cause quite small fiber misalignments (between 1° and 5°), wood rays introduce large local misalignments, with measured values of 27.7° for beech and 15.6° for spruce, for example.

Poulsen et al. (1997) were the first to carry out an exhaustive study of the compressive behavior of clear wood in relation with kink band formation. The overall stress–strain response of wood helped identify three distinct stages of kinking in that material: incipient kinking, transient kinking and steady-state kinking (Fig. 2). During the first stage, kinking initiates near ray cells scattered throughout the material. It remains localized in regions where highly misaligned fibers are under plastic shearing and buckling. The second stage takes place when the stress drops from its peak level to a steady state. During this process, the small regions of incipient kinking grow and coalesce to form a single dominant band across the specimen. Within the band, the fibers are subjected to both compression and large rotation until the lock-up angle is attained and prevents this mode of deformation

* Tel.: +33 (0)1 39 25 42 12; fax: +33 (0)1 39 25 30 15.
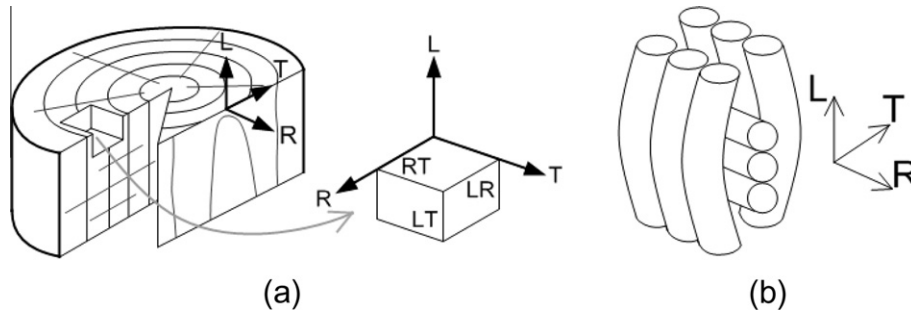 *E-mail address:* lahouari.benabou@uvsq.fr

Fig. 1. (a) Material orientation in wood. (b) Distortion of longitudinal fibers around the ray cells.
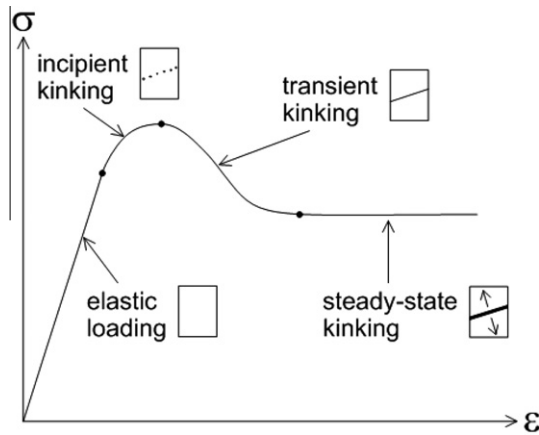

Fig. 2. Schematic diagram of a stress–strain crushing response of wood specimen with the various stages of kinking.

due to volumetric constraints. The last stage occurs under constant applied stress, also called steady state stress. During this regime, the band broadens laterally into the surrounding material. The straight fibers just outside the band are indeed rotated and axially compressed resulting in the observed broadening of the band. In the case of beech and spruce species studied in Benabou (2008), post-test examinations of the failure surface of specimens confirm that large rotation of the fibers occurs within the kink band, as well as some axial deformation that causes buckling of the fibers (Fig. 3a and b). From these observations with microscopy, it is also revealed that micro-cracks are present in the kink band. The inter-fiber failure is the result of the combined effect of shear deformation and transverse tension prevailing in the band. Under these

modes of deformation, wood exhibits a quasi-brittle behavior, i.e. there is a size effect and, at the kink band micro-scale, the true stress–strain curves are characterized by a softening branch after the peak stress (Yamasaki and Sasaki, 2004; Miyauchi and Murata, 2007; Benabou, 2010).

The objective of this paper is to simulate numerically the kink band formation in wood based on a smeared-out plane constitutive model. In Section 2, an anisotropic stress-based criterion (Weihe et al., 1998) is specialized for the fracture process observed in the kinked region and all variables relevant for the initiation and evolution of the wood degradation are described. The smeared fictitious crack approach is used with the criterion to formulate the micro-cracking process. It is shown how this approach makes it possible to use the well established concepts of classical plasticity to treat the kinking failure. In Section 3, the algorithmic implementation of the constitutive model is presented first in the framework of conventional infinitesimal plasticity according to the standard predictor–corrector algorithm and the Newton–Raphson iteration scheme. In Section 4, an extension to finite strain is then made in order to treat large rotation conditions in the kinked material. The formulation makes use of the rotated frame defined by the fiber direction so that the evolution of the directions of orthotropy is strictly described during the kinking process. This approach, quite novel in the treatment of large deformation for wood, is implemented as a user subroutine in the finite element code ABAQUS. Details of the computational steps to process finite rotation at a material point are given at the end of the section. In Section 5, the paper concludes with numerical simulations of kink band formation in beech and spruce species. The model does include a global imperfection based on the measured values of fiber misalignments in wood and the outputs are compared with the results of a previous experimental study carried out by the author.
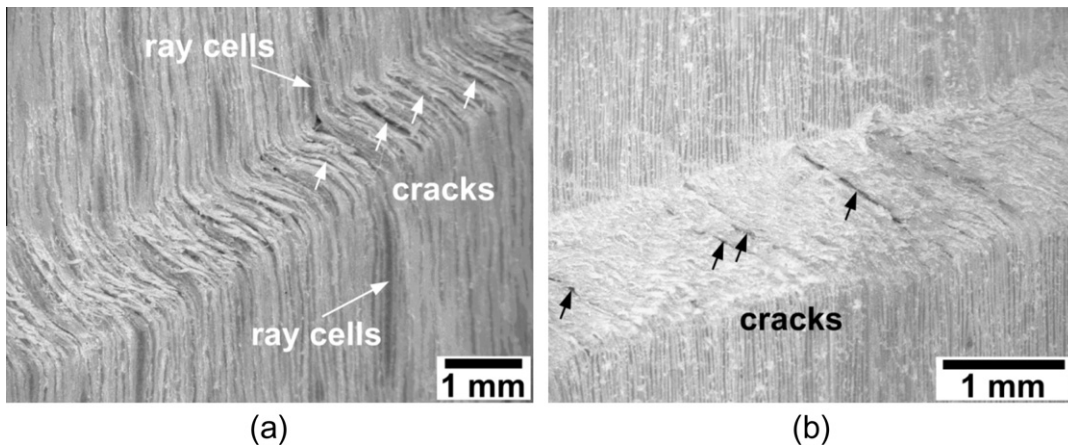

Fig. 3. Post-test observations with microscopy of kink bands in *LT*-plane: (a) beech and (b) spruce.

2. Anisotropic failure criterion

2.1. Initiation of failure

The failure mode observed in combined transverse/shear loading of wood is characterized by cracking parallel to grain and mixed mode I/mode II crack development. In order to describe this mode of failure observed in the kinked region, where mixed mode of shear/transverse deformation occurs, the criterion of Weihe et al. (1998) will be used here. Initially developed for materials like soil, this criterion was successfully applied to the modeling of anisotropic failure in spruce wood by Lucena-Simon et al. (2000) and serves also as basis in Mackenzie-Helnwein et al. (2003) to describe failure of wood under mixed mode of radial tension and shear. Under plane stress or plane strain conditions, the criterion (Fig. 4) is given in terms of stress components on the considered failure plane, i.e. the stresses σ_T and τ_{LT}:

$$f(\boldsymbol{\sigma}, \mathbf{q}) = -(\sigma_T - q_n - a)^2 + \frac{\tau_{LT}^2}{\tan^2 \varphi} + a^2 \qquad (1)$$

where q_n is the current tensile strength in the T-direction (perpendicular to the crack), a is a stress type parameter which is uniquely related to the current shear strength q_t (parallel to the crack),

$$a = \frac{1}{2} q_n \left(\frac{(q_t/q_n)^2}{\tan^2 \varphi} - 1 \right) \geqslant 0 \qquad (2)$$

and $\tan \varphi$ is the friction coefficient of the surface of a fully developed crack. These parameters define a hyperbolic yield function. Micro-cracking is initiated when $f = 0$; which characterizes the ultimate load that the material can withstand without further degradation. Before crack initiation, the failure criterion obeys the material parameters of the undamaged material, q_{n0} and q_{t0}. For the angle of residual friction, a value of 25°, found in Mackenzie-Helnwein et al. (2003), will be taken for both species. As the crack develops, there is a change in the location and the shape of the failure criterion, as it will be described more precisely in the following sub-sections. Pure mode I failure causes total loss of tensile strength but leaves a rougher interface than mode II failure, as can be seen on the compressive side of Fig. 4.

2.2. Smeared crack approach

To preserve the continuity of the displacement field in the finite element solution, a discrete crack is homogenized and simulated by plastic strains distributed over a finite area. This approach, based on the so-called smeared crack concept, consists in considering the crack behavior in terms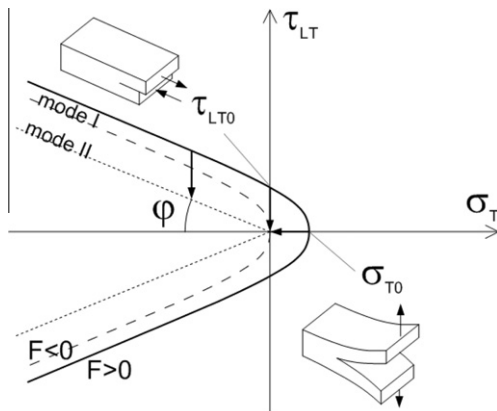 of stress–strain relationships. In this context, Oliver (1989) proposed to define the actual crack band width by a material parameter, referred to as characteristic length ℓ_c. Thus, the degradation of the material can be modeled by inelastic deformations following the concepts of classical elasto-plasticity (Weihe et al., 1998; Ohmenhäuser et al., 1999). The inelastic strain-like parameters $\boldsymbol{\varepsilon}^p$, interpreted as equivalent plastic strains, are formulated according to a "flow" rule:

$$\dot{\boldsymbol{\varepsilon}}^p = \dot{\mathbf{u}}^{cr}/\ell_c = \dot{\lambda} \mathbf{m}, \quad \mathbf{m} = \mathbf{A} \cdot \frac{\partial \mathbf{f}}{\partial \boldsymbol{\sigma}} \qquad (3)$$

where $\mathbf{u}^{cr} = [u_n^{cr}, u_t^{cr}]$ is the crack opening/sliding which is directly related to the flow $\dot{\lambda} \mathbf{m}$, with $\dot{\lambda}$ being the consistency parameter. The associated Kuhn–Tucker conditions read:

$$\mathbf{f} \leqslant 0, \quad \dot{\lambda} \geqslant 0, \quad \dot{\lambda} \mathbf{f} = 0 \qquad (4)$$

The transformation matrix $\mathbf{A}$ is used to provide for a pressure dependent dilatation:

$$\mathbf{A} = \begin{bmatrix} \eta & 0 \\ 0 & 1 \end{bmatrix}, \quad \eta = \eta_c \exp \left(-\eta_p \frac{q_{t,r}}{q_{n0}} \right) \qquad (5)$$

The parameter η_p realizes a decreasing dilatation with increasing normal compressive stress on the crack and thus, the dilatation is asymptotically suppressed under high confining stresses. A constant reduction of the dilatation, activated for compressive as well as for tensile normal stress on the crack, can be provided by $\eta_c < 1$. As for the parameter $q_{t,r}$, it represents the residual shear strength.

2.3. Crack evolution

In analogy to fracture mechanics, the softening behavior, resulting from the development of the crack, is governed by the fracture toughnesses (energy release rates) G_f^I and G_f^{II}, for modes I and mode II respectively. With respect to the associated failure mode, the fracture toughness is understood as the energy which is dissipated from initiation of failure to complete separation. Assuring that the energy dissipated due to friction is excluded, this transforms into:

$$G_f^I = \int_{u_n^{cr}=0}^{\infty} \sigma_T du_n^{cr} \big|_{\substack{\tau_{LT}=0 \\ du_n^{cr}>0}}$$
$$G_f^{II} = \int_{u_t^{cr}=0}^{\infty} (|\tau_{LT}| - q_{t,r}) |du_t^{cr}| \big|_{\sigma_T=0} \qquad (6)$$

Two normalized internal state variables, expressed with respect to the inelastic strains rather than the crack opening displacements, are introduced to describe the dissipated energy for each failure mode:

$$\dot{\xi}^I = \frac{\ell_c}{G_f^I} \sigma_T \langle \dot{\varepsilon}_T^p \rangle = \frac{\ell_c}{G_f^I} \sigma_T \langle m_n \rangle \dot{\lambda}$$
$$\dot{\xi}^{II} = \frac{\ell_c}{G_f^{II}} (|\tau_{LT}| - q_{t,r}) |\dot{\gamma}_{LT}^p| = \frac{2\ell_c}{G_f^{II}} (|\tau_{LT}| - q_{t,r}) |m_t| \dot{\lambda} \qquad (7)$$

where $\langle x \rangle = (x + |x|)/2$. The residual shear strength is also taken into account through:

$$q_{t,r} = \langle -\sigma_T \tan \varphi \rangle \qquad (8)$$

ensuring that the energy under mode II which is dissipated due to friction is excluded. The post-failure behavior of wood is then described with the evolution laws of the strength values:

$$q_n = (1 - \kappa_n) q_{n0}, \quad \kappa_n = \min(1, \xi^I + \xi^{II})$$
$$a = (1 - \kappa_a) a_0, \quad \kappa_a = \xi^{II} \qquad (9)$$

The failure in mode I leads to a complete decohesion by reducing the tensile strength q_n to zero. However, degradation under this mode

Fig. 4. Micromechanical description of mixed mode failure observed in the kinked material.

does not affect the roughness of the surface and thus, the asperity parameter remains constant. The failure in mode II decreases the tensile strength and grinds off the asperities as well. Therefore, shear failure affects both the tensile strength q_n and the asperity parameter a. The strength degradation, which could be obtained by integrating Eq. (7), can be shown to follow an exponential decay with respect to the corresponding crack opening/sliding.

2.4. Localization limiter and characteristic length

Within the local approach of softening cracking, the material behavior usually localizes and the mesh size may have an influence on the numerical results. By using the localization band width ℓ_c proportional to the size of the finite elements, an energetically consistent framework is established. The fracture toughnesses are substituted by element specific values G_f^I/ℓ_c and G_f^{II}/ℓ_c and thus, the description parameters relevant to degradation are the plastic strains rather than the crack opening displacements, as written in Eq. (7). Therefore, in the simulation of structural degradation processes, the same amount of dissipated energy is computed independent of the element size, alleviating the mesh dependency of the results. Also, uniaxial investigations of wood behavior in Mackenzie-Helnwein et al. (2003) show that the characteristic length must not exceed an upper limit so that the behavior of the model remains physically relevant. Considering uniaxial tension in T-direction, as is the case within the kinked region, yields to the following constraint:

$$\ell_c < \ell_{c,critical} = \frac{E_T G_f^I}{q_{n0}^2} \tag{10}$$

The band width ℓ_c may be the length of a finite element perpendicular to the crack direction and so, Eq. (10) states that if the element size exceeds $\ell_{c,critical}$, instant loss of stiffness may be observed.

3. Numerical implementation for infinitesimal plasticity

3.1. Integration of equilibrium equations

The finite element discretization of the momentum balance equation for the system is carried out based on the dynamic explicit approach. The nonlinear equation can be expressed as follows:

$$\boldsymbol{M} \cdot \ddot{\boldsymbol{u}} + \boldsymbol{F}^{int} = \boldsymbol{F}^{ext} \tag{11}$$

where $\boldsymbol{M}$ is the mass matrix, $\boldsymbol{F}^{int}$ and $\boldsymbol{F}^{ext}$ are the vectors of the internal and external forces, respectively. The integration of the equation is made using the central difference time integration scheme, available in ABAQUS/Explicit. The acceleration term at time t_n is obtained with Eq. (11):

$$\ddot{\boldsymbol{u}}_n = \boldsymbol{M}^{-1} \cdot (\boldsymbol{F}_n^{ext} - \boldsymbol{F}_n^{int}) \tag{12}$$

From this relation, the mid-step velocity term, for time $t_{n+1/2}$, can be defined as follows:

$$\dot{\boldsymbol{u}}_{n+1/2} = \dot{\boldsymbol{u}}_{n-1/2} + \frac{\Delta t_n + \Delta t_{n+1}}{2} \ddot{\boldsymbol{u}}_n \tag{13}$$

with Δt_{n+1} the time increment between t_n and t_{n+1}, and Δt_n being defined similarly. Finally, the displacement term is calculated at time t_{n+1} according to the formula:

$$\boldsymbol{u}_{n+1} = \boldsymbol{u}_n + \Delta t_{n+1} \dot{\boldsymbol{u}}_{n+1/2} \tag{14}$$

Based on the element-by-element estimate, the stability condition for the time increment can be expressed with respect to the characteristic element length ℓ_c and the wave speed of the material $c_d = \sqrt{E/\rho}$:

$$\Delta t \leqslant \frac{\ell_c}{c_d} \tag{15}$$

3.2. The implicit elastic predictor/return-mapping scheme

The numerical implementation of the proposed constitutive model within the infinitesimal plasticity framework is based on the return mapping algorithm as generalized by Simo and Hughes (1998). Some details are also found in Mackenzie-Helnwein et al. (2003, 2005) for a more general orthotropic elastoplastic model applied to wood. The Fortran user subroutine in ABAQUS/Explicit, called VUMAT, is used to implement the plasticity constitutive equations. All quantities are known at time t_n (initial conditions) and they are to be determined at time t_{n+1}, with the exception of the total strain ε_{n+1} which is assumed to be known from the current solution for the global displacement field. The backward (or fully implicit) Euler scheme is adopted to integrate the plastic flow rule (Eq. (3)), the evolution equations for the softening parameters (Eq. (7)), and the Kuhn–Tucker conditions (Eq. (4)). The prescribed incremental strain being $\Delta\varepsilon_{n+1} = \varepsilon_{n+1} - \varepsilon_n$ for the current step, the following discretised system has to be solved:

$$\begin{aligned}\Delta\boldsymbol{\varepsilon}_{n+1}^e &= \Delta\boldsymbol{\varepsilon}_{n+1} - \Delta\lambda_{n+1}\boldsymbol{m}_{n+1} \\ \Delta\boldsymbol{\xi}_{n+1} &= \Delta\lambda_{n+1}\boldsymbol{K}_{n+1}\end{aligned} \tag{16}$$

for the unknowns $\Delta\boldsymbol{\varepsilon}_{n+1}^e$, $\Delta\boldsymbol{\xi}_{n+1}$, and $\Delta\lambda_{n+1}$ subjected to the constraints:

$$f(\boldsymbol{\sigma}_{n+1}, \boldsymbol{q}_{n+1}) \leqslant 0, \quad \Delta\lambda_{n+1} \geqslant 0, \quad \Delta\lambda_{n+1}\boldsymbol{f}(\boldsymbol{\sigma}_{n+1}, \boldsymbol{q}_{n+1}) = 0 \tag{17}$$

In Eq. (16), $\boldsymbol{m}_{n+1} = \boldsymbol{A}\partial_\sigma f(\boldsymbol{\sigma}_{n+1}, \boldsymbol{q}_{n+1})$ is the plastic flow direction of the surface and $\boldsymbol{K}_{n+1}$ are factors derived from the relationships in Eq. (7). The softening rules, giving the evolution of $\boldsymbol{\xi} = \lfloor \xi^I, \xi^{II} \rfloor$, directly involve the stresses at $t = t_{n+1}$ and are solved according to an implicit scheme in this study, making a difference with the explicit scheme used in Mackenzie-Helnwein et al. (2003). At the end of the time step, the computation of the other variables is eventually made using the elastic stress–strain relationship and the evolution laws for the strength functions:

$$\begin{aligned}\boldsymbol{\sigma}_{n+1} &= \boldsymbol{\sigma}_n + \boldsymbol{C} : \Delta\boldsymbol{\varepsilon}_{n+1}^e \\ \boldsymbol{q}_{n,n+1} &= (1 - \kappa_{n,n+1})\boldsymbol{q}_{n0}, \quad \boldsymbol{a}_{n+1} = (1 - \kappa_{a,n+1})\boldsymbol{a}_0\end{aligned} \tag{18}$$

The sets of equations are solved following a two-step algorithm (Fig. 5):

- The *Elastic Trial Step* is defined by the previous equations with $\Delta\lambda_{n+1} = 0$. If $f(\boldsymbol{\sigma}_{n+1}, \boldsymbol{q}_{n+1}) \leqslant 0$, the solution is assumed purely elastic and the unknowns at the end of the step are given by:

$$\begin{aligned}\Delta\boldsymbol{\varepsilon}_{n+1}^{e\,trial} &= \Delta\boldsymbol{\varepsilon}_{n+1} \\ \Delta\xi_{n+1}^{trial} &= 0\end{aligned} \tag{19}$$

- The *Plastic Corrector Step* is required when $f(\boldsymbol{\sigma}_{n+1}, \boldsymbol{q}_{n+1}) > 0$. The unknowns $\Delta\boldsymbol{\varepsilon}_{n+1}^e$, $\Delta\boldsymbol{\xi}_{n+1}$ and $\Delta\lambda_{n+1}$ are obtained by solving the system given in Eq. (20) according to the standard iterative procedure of Newton–Raphson:

$$\boldsymbol{r}_{n+1} = \begin{Bmatrix} \Delta\boldsymbol{\varepsilon}_{n+1}^e - \Delta\boldsymbol{\varepsilon}_{n+1}^{e\,trial} + \Delta\lambda_{n+1}\boldsymbol{m}_{n+1} \\ \Delta\boldsymbol{\xi}_{n+1} - \Delta\lambda_{n+1}\boldsymbol{K}_{n+1} \\ \boldsymbol{f}(\boldsymbol{\sigma}_{n+1}, \boldsymbol{q}_{n+1}) \end{Bmatrix} = \begin{Bmatrix} \boldsymbol{0} \\ \boldsymbol{0} \\ \boldsymbol{0} \end{Bmatrix} \tag{20}$$

The gradients of the residual $\boldsymbol{r}_{n+1}$ have to be computed with respect to the unknowns $\boldsymbol{x}_{n+1} = \{\Delta\boldsymbol{\varepsilon}_{n+1}^e \Delta\boldsymbol{\xi}_{n+1} \Delta\lambda_{n+1}\}^T$ so that a correction for the known approximation of the solution at the iteration k may be obtained following the procedure in Eq. (21). This iterative procedure is repeated until the condition in Eq. (20) is verified with a satisfactory tolerance. The dot product represents the appropriate multiplication operator for the involved scalars, vectors and tensors.
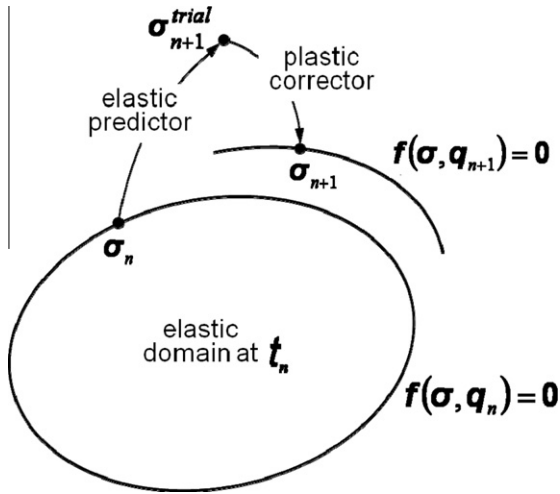
Fig. 5. General return mapping scheme for plasticity.

$$r_{n+1}^{(k)} + \partial_x r_{n+1}^{(k)} \cdot \delta x^{(k+1)} = \mathbf{0} \Rightarrow \delta x^{(k+1)} = -(\partial_x r_{n+1}^{(k)})^{-1} \cdot r_{n+1}^{(k)}$$
$$x_{n+1}^{(k+1)} = x_{n+1}^{(k)} + \delta x^{(k+1)} \tag{21}$$

4. Extension to finite strain elastoplasticity

4.1. Large deformation analysis of fibrous materials

The material in the kinked region undergoes large shear angles causing material nonlinearities. In addition, the rigid body rotation part of the motion, which is significant in kinking failure, plays also a crucial role in the nonlinear behavior. Thus, it is necessary to formulate the elastoplastic model under large deformation conditions. In this context, rate constitutive equations (or hypo-elastic laws) are widely used (Belytschko et al., 2000) and an objective stress rate is employed to ensure the frame indifference of the constitutive response of the material. Classically, co-rotational stress rates, such as the Green–Naghdi or the Jaumann objective derivates, are used because they allow to remove that part of the total stress rate due to simple rigid rotation of the material. However, these derivates use rotations that are mean values of the material rotations and are well adapted for finite strain calculations of isotropic media like metals. In the case of fibrous media, such as wood, the fiber orientation does not follow the orientation of the frames associated to the previously mentioned objective derivates. To take into account this particular point for wood, we use a method derived from studies in the field of woven materials. One of the most frequently used approach for these materials consists in performing the calculations in the rotated frame (Green–Naghdi or Jaumann frame) with the quantities necessary for the incremental computation obtained, by a change of base, from their specific form in the fiber frame (Dong et al., 2001; Peng and Cao, 2005). The alternative approach, which has been proven to be preferable (Badel et al., 2008), consists in using another objective derivate defined from the fiber rotation (Hagege et al., 2005; Boisse et al., 2005). In the present work, the second approach is chosen to describe wood behavior under large deformation and is extended to account for the plasticity formulation developed in Section 3.

4.2. Formulation of the hypo-elastic law accounting for fiber rotation

First, the basic elements of the rate-based model, which are analogous to those of the infinitesimal theory, are presented. Working in the spatial configuration and assuming that the elastic strains are small compared to the plastic strains, the following decomposition of the rate of deformation D, generally used in the implementation of finite plasticity models into finite element codes, is used:

$$D = D^e + D^p \tag{22}$$

where D^e and D^p are the elastic and plastic parts, respectively. The hypo-elastic relation, coupling the objective stress rate with the rate of elastic deformation, is given by:

$$\sigma^{\nabla} = C : (D - D^p) \tag{23}$$

In Eq. (23), C is the elastic stiffness tensor, and σ^{∇} is the objective stress rate of the Cauchy stress. The specificity of this objective rate lies in the use of a rotation tensor based on the fiber rotation Λ (Boisse et al., 2005; Badel et al., 2008) and its definition is given by:

$$\sigma^{\nabla} = \Lambda \cdot \left(\frac{d}{dt}(\Lambda^T \cdot \sigma \cdot \Lambda) \right) \cdot \Lambda^T = \dot{\sigma} - \Omega \cdot \sigma + \sigma \cdot \Omega \tag{24}$$

in which $\Omega = \dot{\Lambda} \cdot \Lambda^T$ is the skew symmetric tensor. When working with FEM, the initial orientation $\{f_i^0\}$ of the orthotropic axes of the material has to be defined relative to the global axes $\{g_i\}$ and this can be expressed with the help of the rotation O:

$$f_i^0 = O \cdot g_i \tag{25}$$

Then, the material rotation Λ is used to update the initial constitutive axes $\{f_i^0\}$ to the current constitutive axes $\{f_i\}$ (Fig. 6):

$$f_i = \Lambda \cdot f_i^0 \tag{26}$$

Whereas the current Green–Naghdi axes $\{e_i\}$ are updated with Eq. (27) using the initial orientation of these axes $\{e_i^0\}$ and the rotation tensor R obtained from the polar decomposition of the deformation gradient tensor F. The directions $\{f_i^0\}$ and $\{e_i^0\}$ are assumed to coincide initially.

$$e_i = R \cdot e_i^0 \tag{27}$$

The material rotation Λ in Eq. (26) is obtained using the procedure given by Crisfield (1997) for large rotations of three-dimensional beams. The developments, made in the context of our study, are detailed in Appendix A. Based on these results, the relations in Eq. (28) give explicitly the constitutive axes $\{f_i\}$ as functions of the initial constitutive axes $\{f_i^0\}$ and the deformation gradient F:
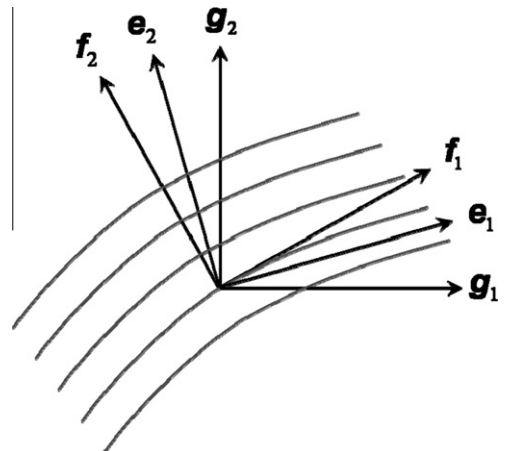

Fig. 6. Green–Naghdi frame rotated by the rotation R and fiber frame rotated by the rotation Λ.

$$f_1 = \frac{\boldsymbol{F} \cdot \boldsymbol{f}_1^0}{\|\boldsymbol{F} \cdot \boldsymbol{f}_1^0\|}$$

$$f_2 = \boldsymbol{f}_2^0 - \frac{b_2}{1+b_1}(\boldsymbol{f}_1^0 + \boldsymbol{f}_1) \tag{28}$$

$$f_3 = \boldsymbol{f}_3^0 - \frac{b_3}{1+b_1}(\boldsymbol{f}_1^0 + \boldsymbol{f}_1)$$

with $b_k = \boldsymbol{f}_1 \cdot \boldsymbol{f}_k^0$ and $b_k \neq 1$. In that formulation, the fiber direction of wood, and so the strong anisotropic direction, remains aligned with the first material direction $\boldsymbol{f}_1$. For a two-dimensional rotation in the 1–2 plane, as is the case with kinking in wood occurring in the *LT*-plane, $\boldsymbol{f}_3 = \boldsymbol{f}_3^0 = g_3$. As for the constitutive behavior, it is fully defined at each time with the help of the initial elastic stiffness tensor $\boldsymbol{C}^0$. The constitutive tensor $\boldsymbol{C}^0$ is computed from the traditional engineer's constants and has the specific form for fibrous materials. In our application, the elastic behavior of wood remains orthotropic during kink banding and is therefore assumed constant when expressed in the fiber frame.

$$\boldsymbol{C}^0 = C_{ijkl}^0 \boldsymbol{f}_i^0 \otimes \boldsymbol{f}_j^0 \otimes \boldsymbol{f}_k^0 \otimes \boldsymbol{f}_l^0 \quad \text{and} \quad \boldsymbol{C} = C_{ijkl}^0 \boldsymbol{f}_i \otimes \boldsymbol{f}_j \otimes \boldsymbol{f}_k \otimes \boldsymbol{f}_l \tag{29}$$

Let us denote now $\boldsymbol{\Theta}$ the rotation between the Green–Naghdi frame $\{\boldsymbol{e}_i\}$, used by ABAQUS, and the material frame $\{\boldsymbol{f}_i\}$:

$$\boldsymbol{\Theta} = \Theta_{ij}\boldsymbol{e}_i \otimes \boldsymbol{e}_j = (\boldsymbol{e}_i \cdot \boldsymbol{\Theta} \cdot \boldsymbol{e}_j)\boldsymbol{e}_i \otimes \boldsymbol{e}_j = (\boldsymbol{e}_i \cdot \boldsymbol{f}_j)\boldsymbol{e}_i \otimes \boldsymbol{e}_j \tag{30}$$

With the definition of this rotation, it becomes possible to transform the strain increments from the Green–Naghdi basis (the work basis of ABAQUS) to the current fiber basis at each time. Then, the update of the stresses is made in the fiber frame and these stresses are expressed back in the Green–Naghdi frame. The details of the stress computation algorithm are given in the following section.

4.3. Stress computation algorithm for finite rotation in wood

To distinguish between the various works bases used in the computations, the tensors expressed in the material frame are denoted by an overbar and those expressed in the Green–Naghdi frame by a hat. In our approach, the stresses are updated in the material frame $\{\boldsymbol{f}_i\}$ and then returned, with a change of base, in the code's work frame of ABAQUS which is the Green-Naghdi frame $\{\boldsymbol{e}_i\}$. Also, it is essential to use an integration algorithm to transform the original time-continuum constitutive equation into an

incremental law satisfying incremental objectivity. This is done by adopting the generalized midpoint rule, related to the Hugues–Winget algorithm (Hughes and Winget, 1980), in which deformation rates are evaluated on the intermediate configuration at time $t_{n+1/2}$. Following this scheme, the stress increments are accumulated in the fiber frame:

$$\bar{\boldsymbol{\sigma}}_{n+1} = \bar{\boldsymbol{\sigma}}_n + \bar{\boldsymbol{C}}_{n+1/2} : \Delta\bar{\boldsymbol{\varepsilon}}_{n+1/2}^e \quad \text{with} \quad \Delta\bar{\boldsymbol{\varepsilon}}_{n+12}^e = \Delta t \bar{\boldsymbol{D}}_{n+1/2}^e \tag{31}$$

In Eq. (31), the elastic stiffness tensor expressed in the fiber frame can be assumed constant as explained before and the stresses $\bar{\boldsymbol{\sigma}}_n$ were calculated during the previous step. Only the term $\Delta\bar{\boldsymbol{\varepsilon}}_{n+1/2}^e$ has to be calculated to compute the stresses at time t_{n+1}. However, the prescribed strain increment is provided by the code in the Green–Naghdi frame, i.e. $\Delta\hat{\boldsymbol{\varepsilon}}_{n+1/2}$, and thus, a change of base must be performed between $\{\boldsymbol{e}_{i,n+1/2}\}$ and $\{\boldsymbol{f}_{i,n+1/2}\}$, requiring to compute the rotation $\boldsymbol{\Theta}_{n+1/2}$. For the sake of simplicity, it is assumed that the time increments are sufficiently small so that the approximation $\boldsymbol{\Theta}_{n+1/2} \approx \boldsymbol{\Theta}_{n+1}$ may be done. The different frames and the rotations needed to obtain these frames are represented at different time increments in Fig. 7. The following procedure describes the computational process performed at each material (Gauss) point during the loading:

- At the beginning of the time step Δt_{n+1}, the code provides the deformation gradient $\boldsymbol{F}_{n+1}$, the right stretch tensor $\boldsymbol{U}_{n+1}$ and the prescribed incremental strains $\Delta\hat{\boldsymbol{\varepsilon}}_{n+1/2}$ in the Green–Naghdi basis.
- Compute the polar rotation tensor using the polar decomposition of the deformation gradient: $\boldsymbol{R}_{n+1} = \boldsymbol{F}_{n+1} \cdot \boldsymbol{U}_{n+1}^{-1}$.
- Compute the current Green–Naghdi basis $\{\boldsymbol{e}_{i,n+1}\}$ using Eq. (27).
- Compute the current material basis $\{\boldsymbol{f}_{i,n+1}\}$ using Eq. (28).
- Compute the rotation $\boldsymbol{\Theta}_{n+1}$ using Eq. (30).
- Compute the prescribed strain increment in the material frame from the code's strain increment: $\Delta\bar{\boldsymbol{\varepsilon}}_{n+1/2} = \boldsymbol{\Theta}_{n+1}^T \cdot \Delta\hat{\boldsymbol{\varepsilon}}_{n+1/2} \cdot \boldsymbol{\Theta}_{n+1}$.
- The term $\Delta\bar{\boldsymbol{\varepsilon}}_{n+1/2}$ defines the material strain increment for use in the conventional small-strain plasticity formulation presented in Section 3. Invoke the elastic predictor/return mapping algorithm, with Eqs. (19)–(21), to calculate the elastic strain increment $\Delta\bar{\boldsymbol{\varepsilon}}_{n+1/2}^e$ and the state variables in the material frame.
- Compute the material stress tensor $\bar{\boldsymbol{\sigma}}_{n+1}$ using Eq. (31).
- Return the material stress tensor in the work code basis: $\hat{\boldsymbol{\sigma}}_{n+1} = \boldsymbol{\Theta}_{n+1} \cdot \bar{\boldsymbol{\sigma}}_{n+1} \cdot \boldsymbol{\Theta}_{n+1}^T$.
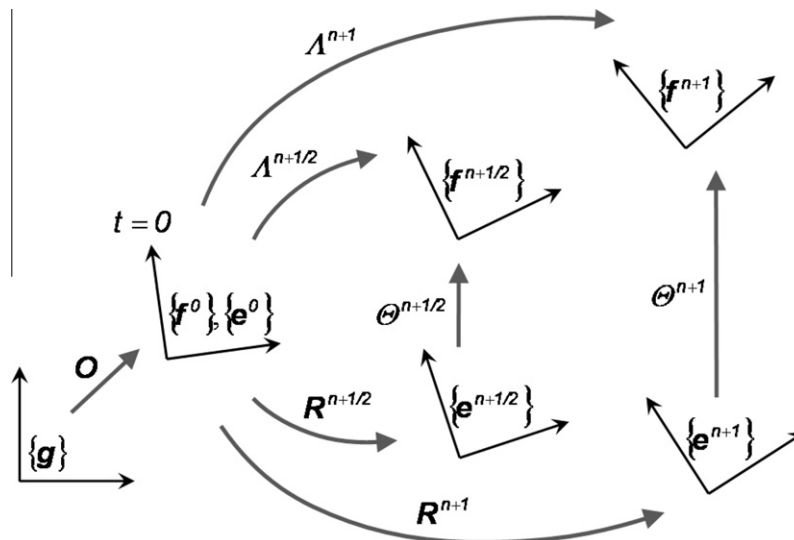

Fig. 7. Green–Naghdi and fiber rotated frames at different time increments.

5. Numerical simulations

5.1. The model parameters

In this section, all the needed parameters for the simulation of kink band formation in wood are presented relatively to the two tested species, beech and spruce wood. Under plane strain conditions, the marked elastic orthotropy of wood species is expressed by the following stress-elastic strain relation referred to the fiber frame:

$$\begin{aligned}\varepsilon_L &= S_{11}\sigma_L + S_{12}\sigma_T \\ \varepsilon_T &= S_{21}\sigma_L + S_{22}\sigma_T \\ \gamma_{LT} &= S_{66}\tau_{LT}\end{aligned} \tag{32}$$

Wood will be assumed to be transversely isotropic, i.e. isotropic in the *RT*-plane, since its behavior in radial and tangential directions is rather similar. Then, the compliances S_{ij} in terms of familiar engineering material parameters are:

$$\begin{aligned}S_{11} &= (1 - v_{LT}v_{TL})/E_L, \quad S_{22} = (1 - v_{RT}^2)/E_T, \\ S_{12} &= S_{21} = -(v_{TL} + v_{TL}v_{RT})/E_T, \quad S_{66} = 1/G_{LT}\end{aligned} \tag{33}$$

The inversion of the system (32) gives the elastic stiffness tensor. The values of the elastic constants, as well as the strengths and the fracture toughnesses, given in Table 1 are used in the simulations. The value of the coefficient v_{TL} is determined by the relation $v_{TL} = v_{LT}E_T/E_L$.

The blocks of wood, used for the simulations, have a height of 20 mm and a cross section of 10 mm × 10 mm with the fiber direction outside the kink band coinciding with the global g_1-axis. Since a dynamic explicit approach is used, the densities of the blocks are taken equal to 680 kg/m³ for beech and 400 kg/m³ for spruce. Four-node plane strain elements with reduced integration are used for the sample discretization. Two different meshes are used for each species to assess the sensitivity of the results to mesh refinement: a 64 × 38 mesh and a 102 × 51 mesh. Examples of meshes,

involving a total of 64 × 38 elements and containing a global imperfection at the center, are given in Fig. 8a and b, for beech and spruce respectively. The models are loaded in longitudinal compression with displacement control by prescribing a velocity of 10 mm/min on the right surface while the left surface remains fixed. In order to ensure quasi-static conditions, the loading is slow enough to eliminate any significant inertia effects. For problems involving brittle failure, this is especially important since the sudden drop in load-carrying capacity, that normally accompanies brittle behavior, leads to increases in the kinematic content of the response. Furthermore, it is known that applying the explicit dynamic procedure to quasi-static problems requires some special considerations because it is often computationally impractical to analyze the problem in its natural time scale. It would indeed require an excessive number of small time increments. To obtain an economical solution, the technique of *mass scaling* has been implemented in our models. Like this, the simulation is accelerated in some way, while keeping the inertial forces insignificant. According to Eq. (15), artificially increasing the material density ρ by a factor f^2 increases the stable time increment by a factor f. Nevertheless, moderate values of mass scaling have been used in the simulations to ensure that correct solutions are found.

As a first approach to model the initial imperfection present in the material and trigger kink band development, the fibers are given the homogeneous inclination in the form of a sinusoidal waviness of the fibers along the g_1-direction (Fig. 9). Referred to as *global imperfection*, the inclination is included according to the expression:

$$v_g = a\left[\sin\left(\frac{\pi\cos\beta}{b}(x_1 + x_2\tan\beta)\right) + 1\right] \tag{34}$$

with amplitude $a = b\tan\phi_0/\pi\cos\beta$ and (x_1, x_2) being the global coordinates. The geometric parameters of the kink band (initial fiber misalignment ϕ_0, band inclination β, band width b) are listed in Table 2. In this first approach, we assume that a long band of misaligned fibers exists in the initial, unstressed state.

Table 1
Material parameters.

| Elastic constants	Longitudinal Young modulus, E_L (MPa)	Transverse Young modulus, E_T (MPa)	Shear modulus, G_{LT} (MPa)	Poisson's ratio, v_{LT}	Poisson's ratio, v_{RT}
Beech	14,000	1160	1038	0.52	0.71
Spruce	11,000	490	740	0.40	0.55
Failure parameters	Tensile strength, q_{n0} (MPa)	Shear strength, q_{t0} (MPa)	Fracture toughness under Mode I G_f^I (N mm^{-1})	Fracture toughness under Mode II, G_f^{II} (N mm^{-1})	
Beech	27.5	24.6	0.73	1.79	
Spruce	12.4	13.1	0.23	0.68	
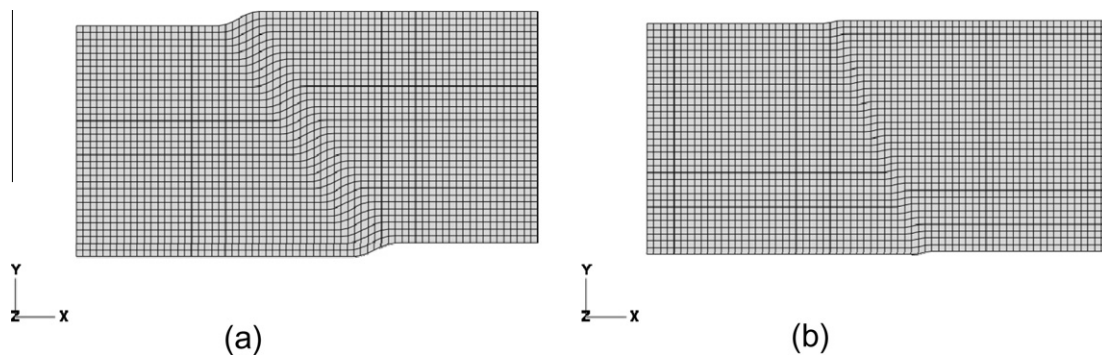
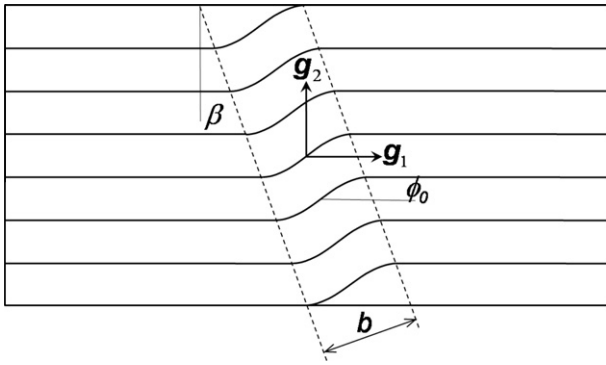**Fig. 8.** F.E. meshes with 64 × 38 elements: (a) beech and (b) spruce.

Fig. 9. Schematics and definition of the kink band geometric parameters.

Table 2
Geometric parameters of the kink band.

Characteristics of the kink band	Fiber misalignment ϕ_0 (°)	Kink band orientation, β (°)	Kink band width, b (mm)
Beech	27.7	30.8	1.6
Spruce	15.6	21.6	0.7

5.2. Load type parameter

In order to characterize clearly the type of loading at a point and for the clarity of the subsequent discussions, the following dimensionless triaxiality factor *T.F.* will be used:

$$T.F. = \frac{3\sigma_H}{\sigma_{eq}} = \frac{\sigma_T}{\sqrt{\sigma_T^2 + 3\tau_{LT}^2}} \qquad (35)$$

with the hydrostatic stress σ_H and the Von Mises stress σ_{eq}. In this formula, the longitudinal stress σ_L along the fiber direction is intentionally not taken into account. It is indeed of limited interest as it is not involved in the failure criterion. Moreover, by considering only the stress components relevant for the degradation process of the material, the parameter *T.F.* is able to give a precise indication of the failure mode characterizing kink banding: mode I and/or mode II crack development. The following specific states can thus be identified in the context of kink band loading:

T.F. = −1 uniaxial compression ($\sigma_T < 0$).
T.F. = 0 pure shear (mode II crack development).
T.F. = +1 uniaxial tension (mode I crack development).

Table 3
Peak stresses obtained from axial compression tests.

Compressive strength	Peak stress, σ_c (MPa)
Beech	51.3 ± 3.2
Spruce	47.4 ± 2.4

5.3. Results

Fig. 10a and b show the material response under compression of the beech and spruce species, respectively. During the compressive deformation, the fiber inclination will increase, resulting in a lower overall stiffness of the material. A localized deformation state is found in the rectangular blocks, indicating a maximum load carrying capacity of approximately 63.1 MPa and 55.3 MPa for beech and spruce, respectively. Although the predictions for the limit load seem to be higher than the corresponding experimental values given in Table 3, they remain relatively in good agreement with the measurements. The implementation of the model does include a material length scale, and consequently the solutions show low mesh dependency with the coarse mesh and the fine mesh giving similar results.

It can also be seen, from Fig. 10a and b, that the load versus shortening curves show more or less pronounced material softening after the peak load is reached, depending on the wood species. For spruce, the material response is more like the behavior of a brittle material with an abrupt stress drop of high magnitude occurring quasi-instantaneously whereas the softening of beech wood appears to be less important. Then, in the post-cracking stage, a clear stiffening of the behavior can be observed for both species; which is indicative of a compressive regime within the kink band during which frictional shear stress can be transferred to the material. As it is well described by the failure criterion presented in Section 2, the already developed crack can indeed transmit shear stress τ_{LT} through friction when it is subjected to compressive normal stress, i.e. $\sigma_T < 0$. This compressive regime along the transverse direction is dominant mainly after the peak load has been reached, at approximately $\delta/L = 0.5\%$ whereas shearing is dominant prior to the peak load as shown by the evolution of the load parameter *T.F.* in Fig. 11a and b.

Along with the deformed meshes, Fig. 12a and b and Fig. 13a and b show a contour plot of the two state variables, ξ^I and ξ^{II}, at the end of the loading for both wood species. These variables, representing the level of degradation under mode I and mode II failure, give many indications of the damage process within the kink band. In the case of beech, shearing is predominantly responsible
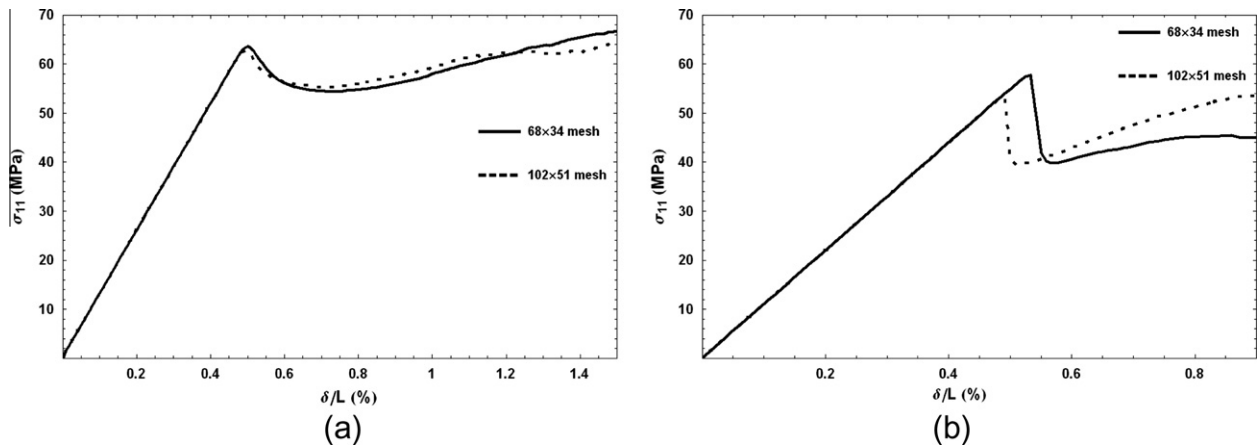

Fig. 10. Axial stress-end displacement response of the 2-D model loaded in pure compression: (a) beech and (b) spruce.

for the degradation occurring in the band as ξ^{II} reaches a value of 0.85 and ξ^{I} attains a lower value of 0.33. In the case of spruce, the levels of degradation caused by shearing and transverse tension are more comparable with critical points being characterized by ξ^{I} = 0.87 and ξ^{II} = 0.96. It is also worth noting that the mode I failure is principally located where fiber curvature is the highest, at the two boundaries of the kink band. In the case of beech, for example, it is seen that transverse tension is high in the zones where the fibers are the most bended (Fig. 14a). This means that

a high level of axial stresses there, resulting logically from the severe local bending, combined with transverse stresses appearing in the same locations, cause the fibers of wood to break in these regions; which constitutes the hinges of the kink band as observed experimentally in Benabou (2008). While transverse tension is located in the boundaries of the kink band, the interior of the kinked domain is characterized by a high compressive stress state; which is also confirmed by the evolution of the triaxiality factor inside the kink band discussed previously. As for
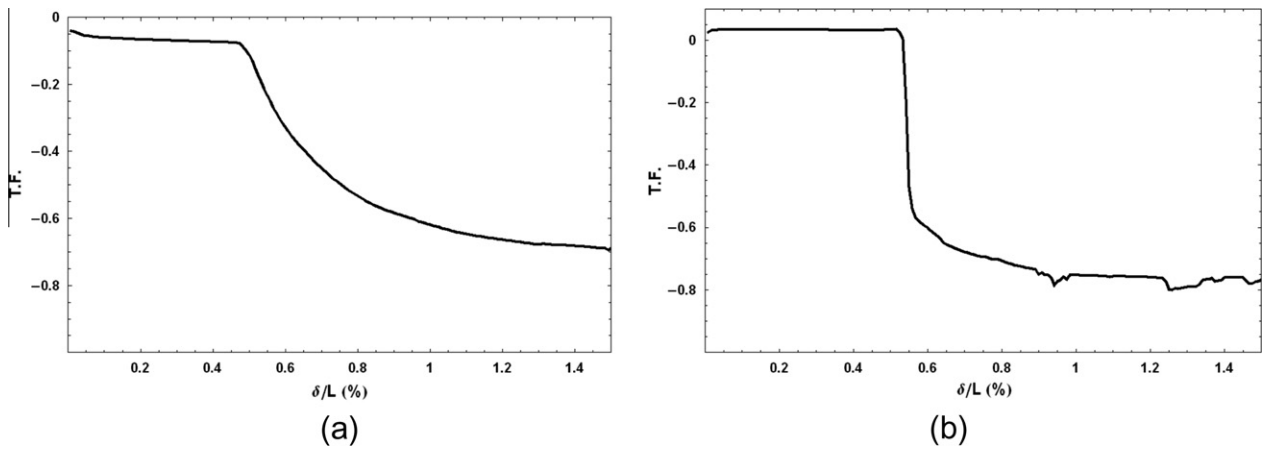

(a)

(b)

Fig. 11. Evolution of the load type parameter during the loading at a material point within the kinked region: (a) beech and (b) spruce.
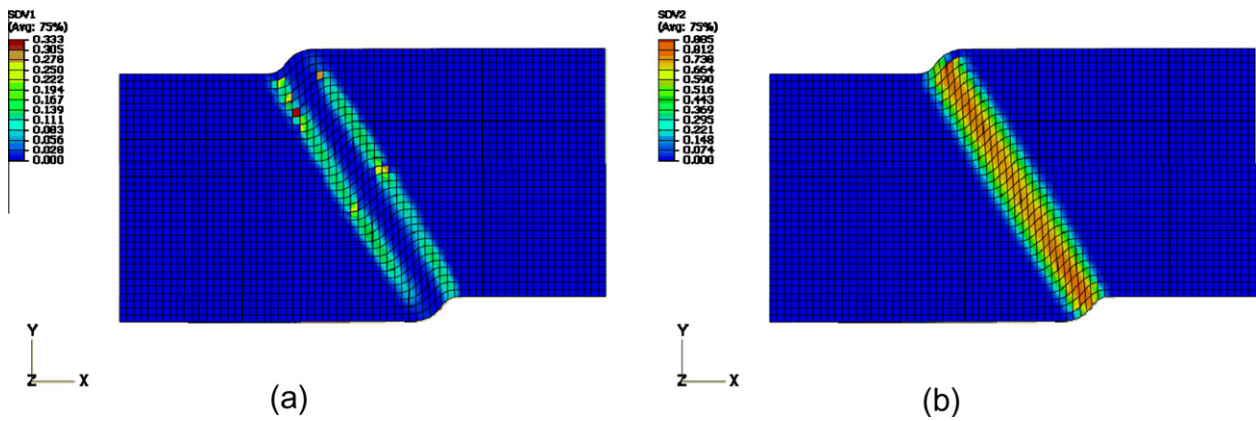

(a)

(b)

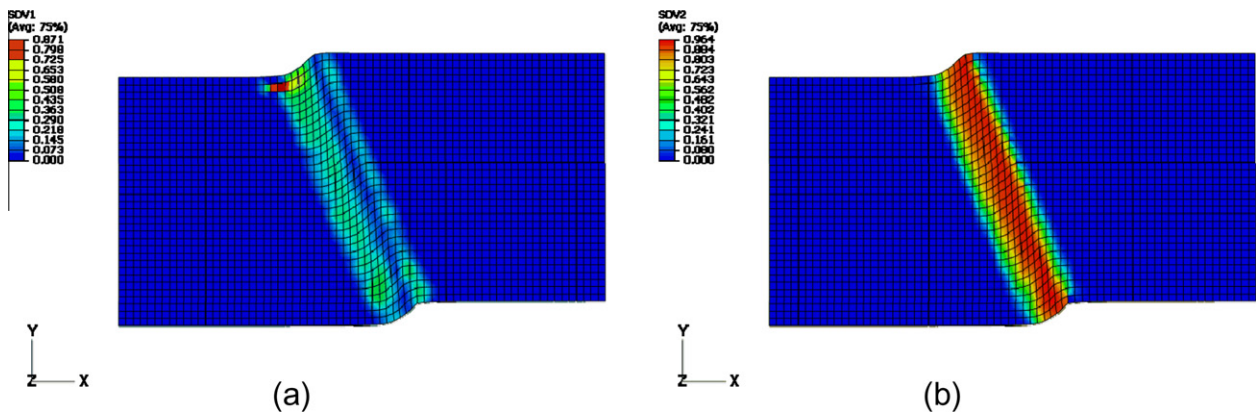**Fig. 12.** Contour plot of the state variables for beech at the end of the compression: (a) ξ^{I} and (b) ξ^{II}.

(a)

(b)

Fig. 13. Contour plot of the state variables for spruce at the end of the compression: (a) ξ^{I} and (b) ξ^{II}.
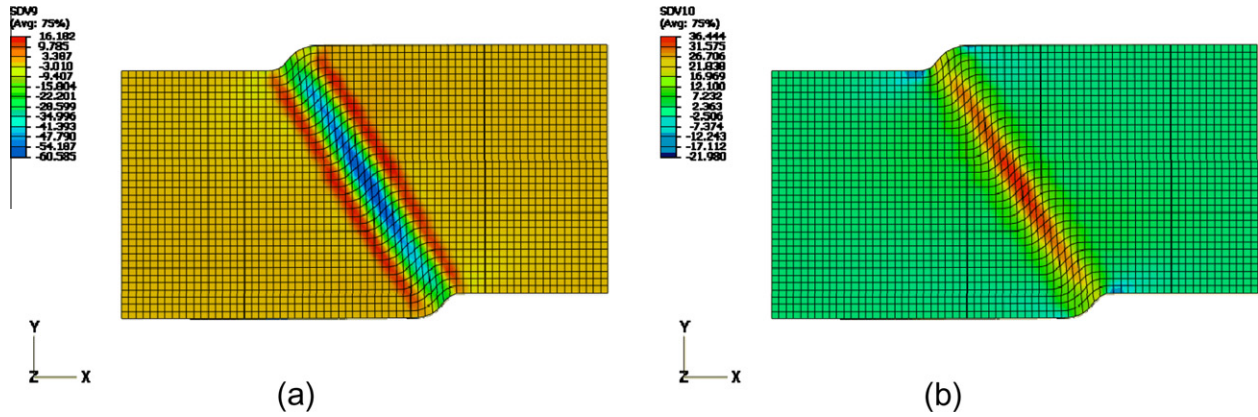
Fig. 14. Transverse stress and shear stress within the beech specimen: (a) σ_T and (b) τ_{LT}.
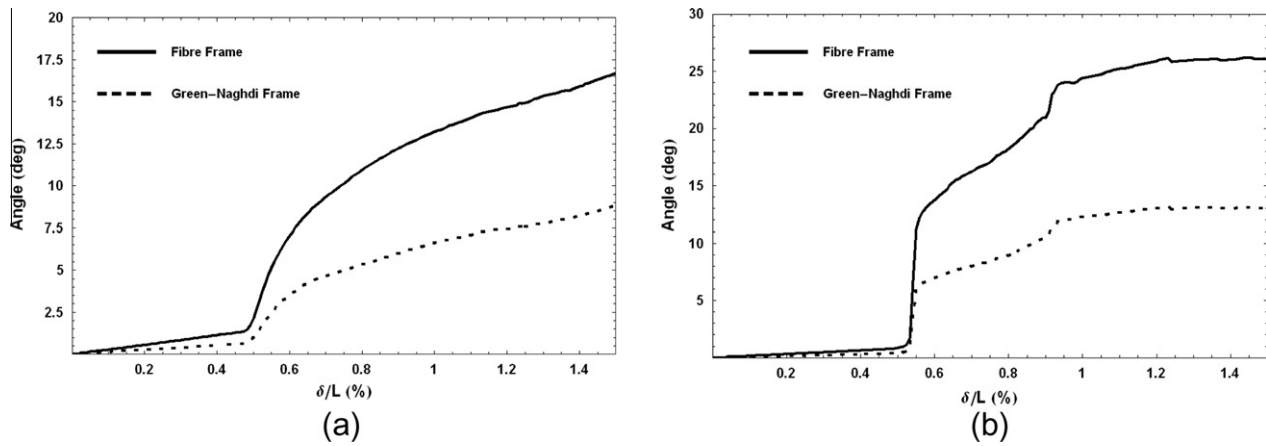

Fig. 15. Comparison for the two approaches of the angle of rotation of the fibers inside the kink band: (a) beech and (b) spruce.
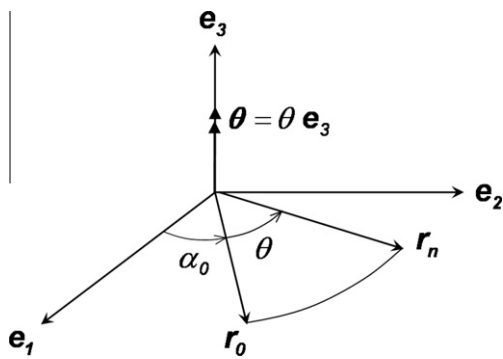

Fig. A.1. Rotation of a vector in the 1–2 plane through θ.

shear stresses, their development takes place to a large extent exclusively within the kink band as illustrated in Fig. 14b in the case of beech.

Finally, the evolution of the angle of rotation of the fibers within the kinked region is plotted according to the Green–Naghdi approach used by default in ABAQUS and the fiber frame approach implemented in ABAQUS using the VUMAT user subroutine (Fig. 15a and b). For both species, the material orientation calculated from the standard polar decomposition of the gradient tensor is largely underestimated at finite strains compared to the orientation obtained by the fiber frame approach. This shows that the classical rotated frame of

Green–Naghdi cannot be used in a satisfactory manner for large strain simulation of fibrous material such as wood. Wood is characterized by a strong anisotropic direction and using an objective derivate defined from the fiber rotation allows to follow as much as possible the matter; which is essential for the correct description of the mechanical behavior during the deformation. Indeed, it was shown that the transverse behavior and shear behavior of wood play a crucial role in kink banding and that large rotation of fibers occurs. So, keeping the orthotropy directions strictly coinciding with fiber directions was essential for obtaining accurate simulation of the studied anisotropic damage mechanism.

6. Conclusion

Kink banding develops in wood subjected to compressive loading in the fiber direction. This mode of failure is responsible for the limitation of the load carrying capacity of wood members under compression and has, thus, to be correctly understood and modeled in the perspective of wood structural design. The degradation process, which takes place in a localized band of fibers undergoing large rotation, is triggered by the initial fiber misalignment naturally present in wood and is characterized by micro-cracking under mixed mode of radial tension and shear. An anisotropic failure criterion is used to describe this mode of rupture observed in the kinked region and is implemented under finite strain conditions in ABAQUS/Explicit using the VUMAT user subroutine. The model, which does include a material length scale, permits to control the

evolution of tensile strength and shear strength by means of two inelastic strain-like parameters representing the crack opening and the relative slip in the interface, respectively. Based on an approach successfully applied to woven materials for the treatment of finite strain conditions, the damage constitutive law of the wood material is expressed in the rate form in the fiber frame to update the tensorial quantities. These quantities are then transformed to the basis of the working code (e.g. Green–Naghdi basis for ABAQUS/Explicit).

Applicability of the model was shown by predicting kinking failure for two wood species with different features, with regards to anatomy, such as fiber misalignment, and to behavior under both shearing and perpendicular-to-grain tension. It is demonstrated that the approach qualitatively predicts the load–displacement curve of wood subjected to compressive failure by providing its load carrying capacity and reproducing the post-cracking behavior. The sequence of events characterizing the kinking phenomenon is also well described. The wood begins deforming globally in an elastic manner until the peak load is reached; then, the material first softens as the deformation localizes into a kink band; finally material softening stops and some stiffening is observed as the compressive state, which develops within the kink band, allows frictional shear stresses to be transferred to the material.

The current developments have been proved to be relatively satisfying for the description of the failure modes of wood under compression and for the simulation of its inelastic behavior in the large strain domain. The computations also pointed out the direction of future enhancements, namely the treatment of kinking propagation by using a small local imperfection instead of a global one. Moreover, the shown examples are encouraging in that future applications can be made in the case of more complex and larger wood structures subjected to compressive failure modes.

Appendix A

A.1. Expression of the rotation characterized by an axis and an angle

During kinking, the wood fibers rotate in the plane 1–2 (*LT*-plane of wood). The rotation is characterized by the vector $\boldsymbol{\theta} = \theta \boldsymbol{e}_3$ where $\boldsymbol{e}_3$ is the unit vector about which the rotation occurs. In Fig. A.1, a vector $\boldsymbol{r}_0$ is rotated in the 1–2 plane through the angle θ to become a vector $\boldsymbol{r}_n$. The following relation between the two vectors can therefore be written:

$$\boldsymbol{r}_n^T = r_0\{\cos(\alpha_0 + \theta), \sin(\alpha_0 + \theta), 0\} \tag{A.1}$$

where $r_0 = ||\boldsymbol{r}_0||$. For small rotations, we can make the approximation:

$$\boldsymbol{r}_n = \left\{ \begin{bmatrix} 1 & 0 & 0 \\ 0 & 1 & 0 \\ 0 & 0 & 1 \end{bmatrix} + \begin{bmatrix} 0 & -\theta & 0 \\ \theta & 0 & 0 \\ 0 & 0 & 0 \end{bmatrix} \right\} \cdot \boldsymbol{r}_0 = [\boldsymbol{I} + \boldsymbol{S}(\theta)] \cdot \boldsymbol{r}_0 \tag{A.2}$$

Thus, from the relation in Eq. (A.2), the rotation matrix for small rotations is given by:

$$\boldsymbol{\Lambda} = \boldsymbol{I} + \boldsymbol{S}(\theta) \tag{A.3}$$

In Eq. (A.3), the tensor $\boldsymbol{S}(\theta)$ operating on the vector $\boldsymbol{r}_0$ can be defined alternately as $\boldsymbol{S}(\theta) \cdot \boldsymbol{r}_0 = \boldsymbol{\theta} \times \boldsymbol{r}_0$ where $\times$ denotes the cross product. For large rotations, the rotation matrix has the exponential form $\boldsymbol{\Lambda} = \exp(\boldsymbol{S}(\theta))$ and the formula of Rodrigues (1840) can be established by expanding the exponential in a power series:

$$\boldsymbol{\Lambda} = \boldsymbol{I} + \frac{\sin(\theta)}{\theta}\boldsymbol{S}(\theta) + \frac{1 - \cos(\theta)}{\theta^2}\boldsymbol{S}(\theta)^2 \tag{A.4}$$

A.2. Particularization of the Rodrigues formula

Let us consider now for our application that $\boldsymbol{r}_0 = \boldsymbol{e}_1^0 = \boldsymbol{f}_1^0$ and $\boldsymbol{r}_n = \boldsymbol{f}_1$ with $\boldsymbol{f}_1 = \boldsymbol{F} \cdot \boldsymbol{f}_1^0 / ||\boldsymbol{F} \cdot \boldsymbol{f}_1^0||$. With this condition, the rotation matrix $\boldsymbol{\Lambda}$ is defined so that the fiber direction of wood, i.e. the strong anisotropic direction, remains aligned with the first vector of $\{\boldsymbol{f}_i\}$. The cosine and the sine of the angle of rotation can be expressed as functions of the axes of the material and initial frames:

$$\cos(\theta) = \boldsymbol{f}_1^0 \cdot \boldsymbol{f}_1$$
$$\frac{\sin(\theta)}{\theta}\boldsymbol{\theta} = \boldsymbol{f}_1^0 \times \boldsymbol{f}_1 \tag{A.5}$$

Using these relations, both terms of the Rodrigues formula can be obtained:

$$\frac{\sin(\theta)}{\theta}\boldsymbol{S}(\theta) = \boldsymbol{S}\left(\frac{\sin(\theta)}{\theta}\boldsymbol{\theta}\right) = \boldsymbol{S}(\boldsymbol{f}_1^0 \times \boldsymbol{f}_1)$$
$$\frac{1 - \cos(\theta)}{\theta^2}\boldsymbol{S}(\theta)^2 = \frac{1}{1 + \boldsymbol{f}_1^0 \cdot \boldsymbol{f}_1}\left(\frac{\sin(\theta)}{\theta}\right)^2 \boldsymbol{S}\left(\frac{\theta}{\sin(\theta)}\boldsymbol{f}_1^0 \times \boldsymbol{f}_1\right)^2 = \frac{1}{1 + \boldsymbol{f}_1^0 \cdot \boldsymbol{f}_1}\boldsymbol{S}(\boldsymbol{f}_1^0 \times \boldsymbol{f}_1)^2 \tag{A.6}$$

which gives, using Eq. (A.4), the following particular form of the material rotation:

$$\boldsymbol{\Lambda} = \boldsymbol{I} + \boldsymbol{S}(\boldsymbol{f}_1^0 \times \boldsymbol{f}_1) + \frac{1}{1 + \boldsymbol{f}_1^0 \cdot \boldsymbol{f}_1}\boldsymbol{S}(\boldsymbol{f}_1^0 \times \boldsymbol{f}_1)^2 \tag{A.7}$$

A.3. Computation of the current material axes

We use the definition in Eq. (A.7) of the material rotation to find the current material axes $\{\boldsymbol{f}_i\}$ as functions of the initial material axes $\{\boldsymbol{f}_i^0\}$ and the deformation gradient $\boldsymbol{F}$:

$$\boldsymbol{f}_1 = \frac{\boldsymbol{F} \cdot \boldsymbol{f}_1^0}{||\boldsymbol{F} \cdot \boldsymbol{f}_1^0||}$$
$$\boldsymbol{f}_2 = \boldsymbol{\Lambda} \cdot \boldsymbol{f}_2^0 = \boldsymbol{f}_2^0 - \frac{b_2}{1 + b_1}(\boldsymbol{f}_1^0 + \boldsymbol{f}_1) \tag{A.8}$$
$$\boldsymbol{f}_3 = \boldsymbol{\Lambda} \cdot \boldsymbol{f}_3^0 = \boldsymbol{f}_3^0 - \frac{b_3}{1 + b_1}(\boldsymbol{f}_1^0 + \boldsymbol{f}_1)$$

with $b_k = \boldsymbol{f}_1 \cdot \boldsymbol{f}_k^0$ and $b_k \neq 1$. For the two-dimensional rotation characterizing the kink banding mechanism, $b_3 = 0$ and so, $\boldsymbol{f}_3 = \boldsymbol{f}_3^0$. To obtain the relations in Eq. (A.8), it was made use of the fact that $\{\boldsymbol{f}_i\}$ and $\{\boldsymbol{f}_i^0\}$ are orthonormal bases and the following property of the cross product was employed:

$$(\boldsymbol{p} \times \boldsymbol{q}) \times \boldsymbol{r} = \boldsymbol{q}(\boldsymbol{p} \cdot \boldsymbol{r}) - \boldsymbol{p}(\boldsymbol{r} \cdot \boldsymbol{q}) \tag{A.9}$$

where $\boldsymbol{p}$, $\boldsymbol{q}$, $\boldsymbol{r}$ are three vectors.

References

Badel, P., Vidal-Sallé, E., Boisse, P., 2008. Large deformation analysis of fibrous materials using rate constitutive equations. Computers and Structures 86, 1164–1175.

Belytschko, T., Liu, W.K., Moran, B., 2000. Nonlinear Finite Elements for Continua and Structures. Wiley.

Benabou, L., 2008. Kink band formation in wood species under compressive loading. Experimental Mechanics 48 (5), 647–656.

Benabou, L., 2010. Predictions of compressive strength and kink band orientation for wood species. Mechanics of Materials 42 (3), 335–343.

Boisse, P., Gasser, A., Hagege, B., Billoet, J.L., 2005. Analysis of the mechanical behavior of woven fibrous material using virtual tests at the unit cell level. Journal of Materials Science 40, 5955–5962.

Budiansky, B., 1983. Micromechanics. Computers and Structures 16 (1), 3–12.

Budiansky, B., Fleck, N.A., 1993. Compressive failure of fibre composites. Journal of the Mechanics and Physics of Solids 41 (1), 183–211.

Budiansky, B., Fleck, N.A., Amazigo, J.C., 1998. On kink-band propagation in fiber composites. Journal of the Mechanics and Physics of Solids 46 (9), 1637–1653.

Christensen, R.M., 2000. Compressive failure of composites using a matrix-controlled failure criterion with the kink band mechanism. Mechanics of Materials 32 (9), 505–509.

Crisfield, M.A., 1997. Non-linear Finite Element Analysis of Solids and Structures. Advanced Topics, vol. 2. Wiley.

Daniel, I.M., Hsiao, H.M., Wooh, S.C., 1996. Failure mechanisms in thick composites under compressive loading. Composites Part B: Engineering 27 (6), 543–552.

Da Silva, A., Kyriakides, S., 2007. Compressive response and failure of balsa wood. International Journal of Solids and Structures 44, 8685–8717.

Dong, L., Lekakou, C., Bader, M.G., 2001. Processing of composites: simulations of the draping of fabrics with updated material behavior law. Journal of Composite Materials 35 (2), 138–163.

Hagege, B., Boisse, P., Billoet, J.L., 2005. Finite element analyses of knitted composite reinforcement at large strain. European Journal of Computational Mechanics 14 (6–7), 767–776.

Hughes, T.J.R., Winget, J., 1980. Finite rotation effects in numerical integration of rate constitutive equations arising in large deformation analysis. International Journal for Numerical Methods in Engineering (15), 1862–1867.

Jensen, H.M., Christoffersen, J., 1997. Kink band formation in fiber reinforced materials. Journal of the Mechanics and Physics of Solids 45 (7), 1121–1136.

Jensen, H.M., 1999. Analysis of compressive failure of layered materials by kink band broadening. International Journal of Solids and Structures 36 (23), 3427–3441.

Kyriakides, S., Arseculeratne, R., Perry, E.J., Liechti, K.M., 1995. On the compressive failure of fiber reinforced composites. International Journal of Solids and Structures 32 (6–7), 689–738.

Lucena-Simon, J., Kröplin, B.H., Dill-Langer, G., Aicher, S., 2000. A fictitious crack approach for the anisotropic degradation of wood. In: Proceedings of the International Conference on Wood and Wood Fiber Composites, Stuttgart, pp. 229–240.

Mackenzie-Helnwein, P., Eberhardsteiner, J., Mang, H.A., 2003. A multi-surface plasticity for clear wood and its application to the finite element analysis of structural details. Computational Mechanics 31 (1–2), 204–218.

Mackenzie-Helnwein, P., Müllner, H.W., Eberhardsteiner, J., Mang, H.A., 2005. Analysis of layered wooden shells using an orthotropic elasto-plastic model for multi-axial loading of clear spruce wood. Computer Methods in Applied Mechanics and Engineering 194, 2661–2685.

Miyauchi, K., Murata, K., 2007. Strain-softening behavior of wood under tension perpendicular to the grain. Journal of Wood Science 53 (6), 463–469.

Moran, P.M., Liu, X.H., Shih, C.F., 1995. Kink band formation and band broadening in fiber composites under compressive loading. Acta Metallurgica et Materialia 43 (8), 2943–2958.

Ohmenhäuser, F., Weihe, S., Kröplin, B., 1999. Algorithmic implementation of a generalized cohesive crack model. Computational Materials Science 16, 294–306.

Oliver, J., 1989. A consistent characteristic length for smeared cracking models. International Journal for Numerical Methods in Engineering 28, 461–474.

Peng, X.Q., Cao, J., 2005. A continuum mechanics-based non-orthogonal constitutive model for woven composite fabrics. Composites: Part A 36, 859–874.

Poulsen, J.S., Moran, P.M., Shih, C.F., Byskov, E., 1997. Kink band initiation and band broadening in clear wood under compressive loading. Mechanics of Materials 25 (1), 67–77.

Rodrigues, O., 1840. Des lois géométriques qui régissent les déplacements d'un système solide dans l'espace et de la variation des coordonnées provenant de ces déplacements considérés indépendamment des causes qui peuvent les produire. Journal de Mathématiques Pures et Appliquées (5), 340–440.

Simo, J.C., Hughes, T.J.R., 1998. Computational Inelasticity. Interdisciplinary Applied Mathematics. Springer.

Sorensen, K.D., Mikkelsen, L.P., Jensen, H.M., 2009. User subroutine for compressive failure of composites. In: SIMULIA Customer Conference, London, pp. 618–632.

Veluri, B., Jensen, H.M., 2010. Simulation of kink band formation in fiber composites. In: Eriksson, A., Tibert, G. (Eds.), 23rd Nordic Seminar on Computational Mechanics, Stockholm, pp. 194–197.

Vogler, T.J., Hsu, S.Y., Kyriakides, S., 2001. On the initiation and growth of kink bands in fiber composites. Part II: Analysis. International Journal of Solids and Structures 38 (15), 2653–2682.

Wadee, M.A., Hunt, G.W., Peletier, M.A., 2004. Kink band instability in layered structures. Journal of the Mechanics and Physics of Solids 52 (5), 1071–1091.

Weihe, S., Kröplin, B., De Borst, R., 1998. Classification of smeared crack models based on material and structural properties. International Journal of Solids and Structures 35 (12), 1289–1308.

Yamasaki, M., Sasaki, Y., 2004. Yield behavior of wood under combined static axial force and torque. Experimental Mechanics 44 (3), 221–227.